RSC Advances

PAPER

View Article Online
View Journal | View Issue

Cite this: *RSC Adv.*, 2023, **13**, 12375

Boron doping effect on the structural, spectral properties and charge transfer mechanism of orthorhombic tungsten bronze β-$SrTa_2O_6$:Eu^{3+} phosphor

Mustafa İlhan *[a] and Lütfiye Feray Güleryüz [b]

In the study, the effect of boron doping on spectral properties and CTB mechanism was investigated by using Eu^{3+} doped orthorhombic β-$SrTa_2O_6$. A phosphor series of Eu^{3+} doped $SrTa_2O_6$, and Eu^{3+} and B^{3+} co-doped $SrTa_2O_6$ polycrystals were fabricated by solid-state reaction at 1400 °C for 20 h in an air atmosphere. The X-ray diffractions of the main phase structure for all the ceramics maintained up to 10 mol% Eu^{3+} concentration, while the increase of XRD intensity for Eu^{3+} and B^{3+} co-doped samples was attributed to somewhat improvement of crystallization. SEM morphologies of grains showed that the presence of boron promotes agglomeration and grain growth. The doping of boron up to 20 mol% led to an increase in PL intensity, CTB energy slightly shifted to low energy, and also an increase occurred in the asymmetry ratio of the phosphor. Therefore, the low crystal field symmetry of the Eu^{3+} sites and some improvement in crystal structure properties for Eu^{3+}, B^{3+} co-doped samples supported the PL increase. The trend of Judd–Ofelt parameters (Ω_2, Ω_4) is $SrTa_2O_6$:$x$$Eu^{3+}$, 0.1$B^{3+}$ > $SrTa_2O_6$:$x$$Eu^{3+}$. The high Ω_2 parameter for boron co-doped samples showed a covalent Eu–O bond character with low symmetry of Eu^{3+} environment, while the high Ω_4 value indicated the reduction in electron density of the ligands. Some increase in the short decays of Eu^{3+}, B^{3+} co-doped samples is probably due to the surface effect and low crystal field symmetry. The quantum efficiency of 0.05Eu^{3+}, 0.1B^{3+} co-doped phosphor with the highest PL intensity increased by about 21% compared to that without boron.

Received 29th January 2023
Accepted 12th April 2023

DOI: 10.1039/d3ra00618b

rsc.li/rsc-advances

1. Introduction

The trivalent europium ion (Eu^{3+}) is known for its strong luminescence in the red spectral region which exhibits interesting theoretical properties. The Eu^{3+} has a great advantage over other RE ions due to the initial levels of transitions in both the absorption and luminescence spectrum not degenerate ($J = 0$).[1,2] The charge transfer (CT) transitions of Eu^{3+} luminescence exhibit broad absorption bands called charge transfer (CT) bands or ligand-to-metal charge transfer (LMCT) bands in the ultraviolet region of electromagnetic spectrum. CT bands occur due to electron transfer where an electron is transferred from one or more neighboring atoms to the Eu^{3+} ion, and Eu^{3+} is formally reduced to Eu^{2+}. The trivalent europium is the most oxidizing of the trivalent rare-earth ions, because Eu^{3+} lacks only one electron to reach a stable half-filled shell.[1] The CT bands are very intense compared to the f–f transitions due to the transitions are allowed by the Laporte selection rule, and the position of the CT bands strongly depends on the nature of the ligands. CT bands can be useful for sensitization of Eu^{3+} luminescence, because they can act as an antenna to absorb light and to transfer the excitation energy to Eu^{3+} ion.[1]

Tungsten bronze (TB) crystal structures are good host matrix candidates for many luminescent applications due to their crystal structure with different coordinated cationic tunnels that allow doping of RE^{3+} ions.[3–7] $SrTa_2O_6$ occurs as three different polymorphs in SrO–Ta_2O_5 system.[6–9] Two polymorphs of $SrTa_2O_6$ are related to TB symmetry and occur at high temperatures. The β-$SrTa_2O_6$ crystallizes at temperatures between 1300–1500 °C, while the β′-$SrTa_2O_6$ forms at temperatures over 1500 °C.[6–9] The other polymorph is orthorhombic α-$SrTa_2O_6$ occurs at about 1100 °C and below. However, the synthesis of α-$SrTa_2O_6$ is difficult with the solid state reaction, so it can be produced by the flux method using strontium borate.[10] Tungsten bronze polymorphs have similar lattice sizes but their crystal symmetries are different. This difference affects its physical properties, that β′-$SrTa_2O_6$ polymorph has better dielectric properties compared to β-$SrTa_2O_6$.[8,9] The β-$SrTa_2O_6$ is orthorhombic with space group *Pnam* and lattice parameters $a = 12.37$ Å, $b = 12.43$ Å, $c = 7.72$ Å, $V = 1187.70$ Å^3, $Z = 10$.[8,9] The β′-$SrTa_2O_6$ is tetragonal with space group *P*4/*mbm* and lattice

[a]*Department of Environmental Engineering, Faculty of Engineering, Marmara University, Kadıköy, 34722, İstanbul, Turkey. E-mail: mustafa.ilhan@marmara.edu.tr*
[b]*Department of Mechanical Engineering, Faculty of Engineering, Ege University, Bornova, 35040, İzmir, Turkey*

parameters $a = 12.47$ Å, $c = 3.90$ Å, $V = 606.27$ Å^3, $Z = 5$.[8,9] The comparison of the two tungsten bronze polymorphs shows that the orthorhombic distortion of β-$SrTa_2O_6$ to β′-$SrTa_2O_6$ is accompanied by an expansion of the TaO_6 octahedral with narrowing of the $(Sr_2)O_{13}$ tricapped pentagonal prisms. Although the crystal lattice of β-$SrTa_2O_6$ is about 2.5% smaller than β′-$SrTa_2O_6$, Ta–O bond distances and corresponding octahedral volumes of β-$SrTa_2O_6$ are large, and it has a relaxed anion sublattice where electrostatic interactions are optimized *via* octahedral tilting distortions.[8]

Boron is widely used as a dopant in glasses to improve its optical and mechanical properties which could promote vitrification of oxide.[11] However, the doping effect of boron has been studied in detail for certain structures such as TiO_2. In boron-doped TiO_2, interstitial B has the more stable form under high calcination temperature compared to substitutional B. An increase and decrease occurred in the lattice parameters are associated with interstitial B and substitutional B, respectively.[12,13] Boron types can take at least two different major positions in TiO_2 which are the oxygen–boron substitution (paramagnetic state), and the interstitial boron (diamagnetic state). In the paramagnetic B arrangement, electrons can be easily captured from other defect states, whereas in the diamagnetic B arrangement, the centers do not transfer charge to other defects in the system. In any case, the driving force for boron to occupy interstitial positions is the formation of very strong bonds with oxygen.[14] The doping of boron to $SrAl_2O_4$:Eu^{2+}, Dy^{3+} phosphor improves the performance of trapping centers and afterglow times at the low temperature.[15] The powders of Eu^{3+} doped $CdNb_2O_6$ and Eu^{3+}, B^{3+} co-doped $CdNb_2O_6$ are prepared by molten salt synthesis method and the presence of orthorhombic single phase without any other interphase showed that boron is incorporated in the host structure and a significant increase occurred in PL.[16]

In the study, the effect of boron doping on the photoluminescence, charge transfer transition, and structural properties of the Eu^{3+} doped β-$SrTa_2O_6$ and Eu^{3+}, B^{3+} co-doped β-$SrTa_2O_6$ phosphors were investigated. The structural and spectroscopic characterizations were carried out by XRD, SEM, XPS, PL, decay time analyses, and also the spectral properties were examined comparatively within the scope of Judd–Ofelt theory.

2. Experimental

$SrTa_2O_6$:xEu^{3+}, yB^{3+} ceramic samples were fabricated in three groups by solid-state reaction. First group contains Eu^{3+} doped samples with x = 0.5, 1.5, 3, 5, 7, 10 mol% concentrations, second group has $x = 5$ mol% Eu^{3+} and $y = 0$, 5, 10, 20 mol% B^{3+} co-doped samples while the third group represents the y = 10 mol% B^{3+} and x = 0.5, 1.5, 3, 5, 7, 10 mol% Eu^{3+} doped samples. Each 1 mol% of x represents two atomic% values of the Eu_2O_3 compound. Strontium carbonate ($SrCO_3$: Sigma-Aldrich, 99%), and tantalum oxide (Ta_2O_5: Alpha Aesar, 99.9%) powders were used as starting materials in calculated stoichiometric amounts. Europium oxide (Eu_2O_3: Alpha Aesar, 99.9%) and boric acid (H_3BO_3: Kimyalab, %99.9) were used as dopant materials. The $SrCO_3$ and Ta_2O_5 were weighed according to the stoichiometry of $SrTa_2O_6$. For CO_2 extraction, $SrCO_3$ was kept in a furnace at 1200 °C for 1 h to obtain SrO. Then SrO and Ta_2O_5 powders were homogenized by mixing well with the addition of acetone in an agate mortar. The powder mixture of SrO and Ta_2O_5 was doped by the 0.5, 1.5, 3, 5, 7, 10 mol% Eu_2O_3 (for the 1st group), 5 mol% Eu_2O_3 and 0, 5, 10, 20 mol% H_3BO_3 (for the 2nd group), 0.5, 1.5, 3, 5, 7, 10 mol% Eu_2O_3 and 10 mol% H_3BO_3 (for the 3rd group), respectively. The final powder mixtures were mixed by acetone for further homogenization. The prepared powders were sintered in an electric furnace at 1400 °C for 20 h after pelleting.

The phase structure of the ceramic samples were examined by XRD (X-ray diffractometer; Bruker D-8 Advance, Bruker Corp., Germany) between 2θ = 20–65 °C using Cu-K_α (1.5406 Å) radiation and scan speed 2 °C min^{-1}. The grain morphology of the ceramic samples was investigated by SEM (scanning electron microscopy; FEG-SEM; XL 30S, Philips Corp., Netherlands). Elemental analysis was performed by the Thermo-Scientific Al-K_α model XPS device. Photoluminescence (PL) results were taken by a fluorescence spectrometer (FLS920, Edinburgh Instruments, UK) equipped with a 450 W ozone-free Xe lamp. Lifetime data were also obtained by fluorescence spectrometer (FLS920) using the time-correlated single-photon counting (TCSPC) system. PL analysis was performed at room temperature.

3. Results and discussions

3.1 Structural analyses

X-ray diffractions of $SrTa_2O_6$:xEu^{3+} samples for x = 0.5, 1.5, 3, 5, 7 10 mol% Eu^{3+} concentrations are shown in Fig. 1. The presence of single-phase continued from 0.5 to 10 mol%, and there was no impurity phase. The crystal symmetry of β-$SrTa_2O_6$ is identified by the first report as *Pbam* (no. 55) and JCPDS card no. 51-1683.[17] However, Lee *et al.*[7] reported that the crystal symmetry is suitable for the space group *Pnam*. Accordingly, the crystal symmetry of the orthorhombic TB samples was indexed with space group *Pnam* (no. 62).[8,9] Tetragonal tungsten bronze structure can be expressed by the $A_4B_2C_4M_{10}O_{30}$ general formula where the pentagonal (A), square (B), and triangular (C) tunnels have 15 CN (large ions such as alkaline earth ions and alkali), 12 CN (such as rare earth ions), 9 CN (small ions such as Li^+), respectively. Also, the octahedral Ta sites with small and highly charged ions have 6 CN.[4–7] The Eu^{3+} ions (r = 1.12 Å, for CN 9) will be suitable for the A and B sites with 15 and 12 CN, respectively. Tungsten bronze symmetry at high concentrations may persist despite of some change occurring in the lattice, which can be attributed to the superiority of TB for RE^{3+} doping.[3–7] In addition, although the β-$SrTa_2O_6$ polymorph has preserved its single-phase structure, it is likely to suffer some increase in distortion due to its slightly longer Ta–O bond distances compared to β′-$SrTa_2O_6$. X-ray diffractions of $SrTa_2O_6$:xEu^{3+}, yB^{3+} ($x = 5$ mol% Eu^{3+}, y = 0, 5, 10, 20 mol% B^{3+}), and $SrTa_2O_6$:xEu^{3+}, yB^{3+} (x = 0.5, 1.5, 3, 5, 7, 10 mol% Eu^{3+}, y = 10 mol% B^{3+}) co-doped samples are shown in Fig. 2a, b and 3, respectively. As seen in the figures, the diffraction peaks of Eu^{3+}, B^{3+} co-doped samples exhibited a slight narrowing compared to

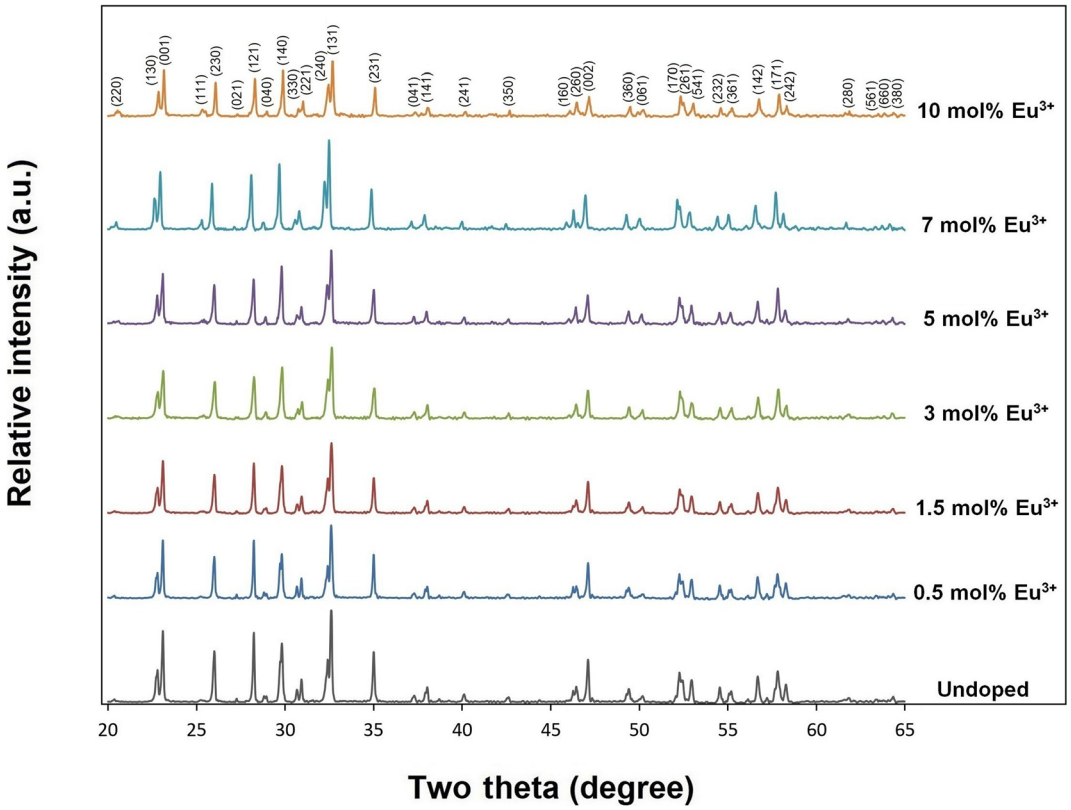

Fig. 1 XRD results of undoped, 0.5, 1.5, 3, 5, 7, and 10 mol% Eu^{3+} doped $SrTa_2O_6$ samples.

the Eu^{3+} doped samples, indicating some improvement in crystallization. The absence of secondary phases in XRD patterns can be also associated with the boron's successful incorporation into the structure. In Fig. 2b, the reflection (131) showed a slight shift towards the smaller two theta angles, which is likely related to the increase in B^{3+} concentration leading to the expansion of the lattice volume.

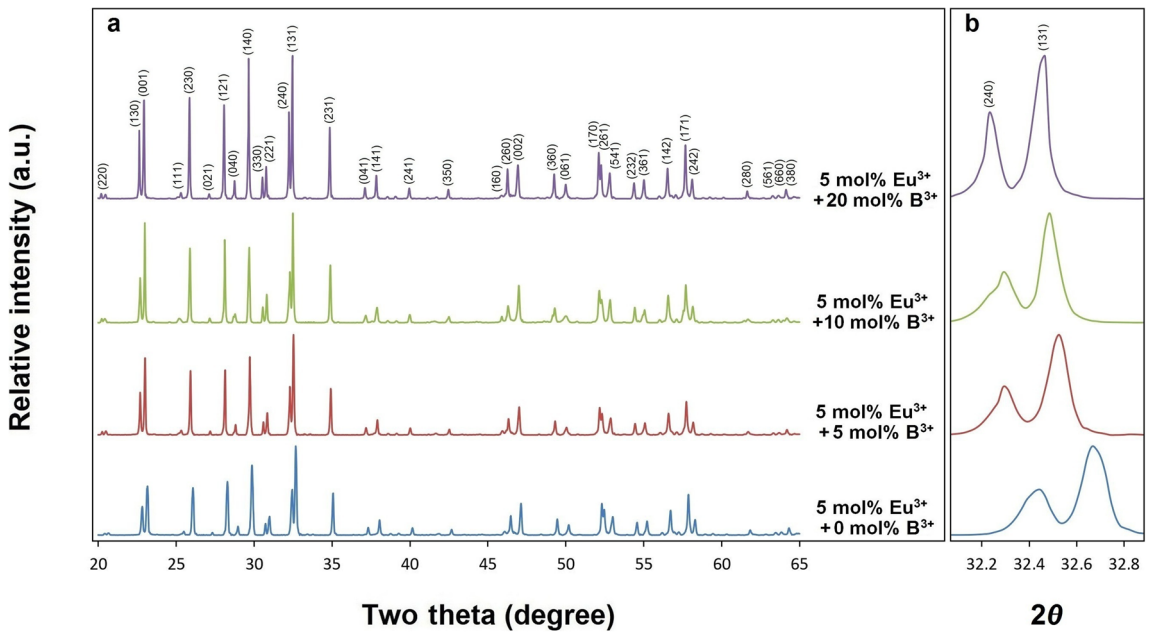

Fig. 2 XRD results of (a) 5 mol% Eu^{3+}, and 0, 5, 10, 20 mol% B^{3+} co-doped $SrTa_2O_6$, (b) the shift of the two theta angle peaks (240) and (131) to lower angles.

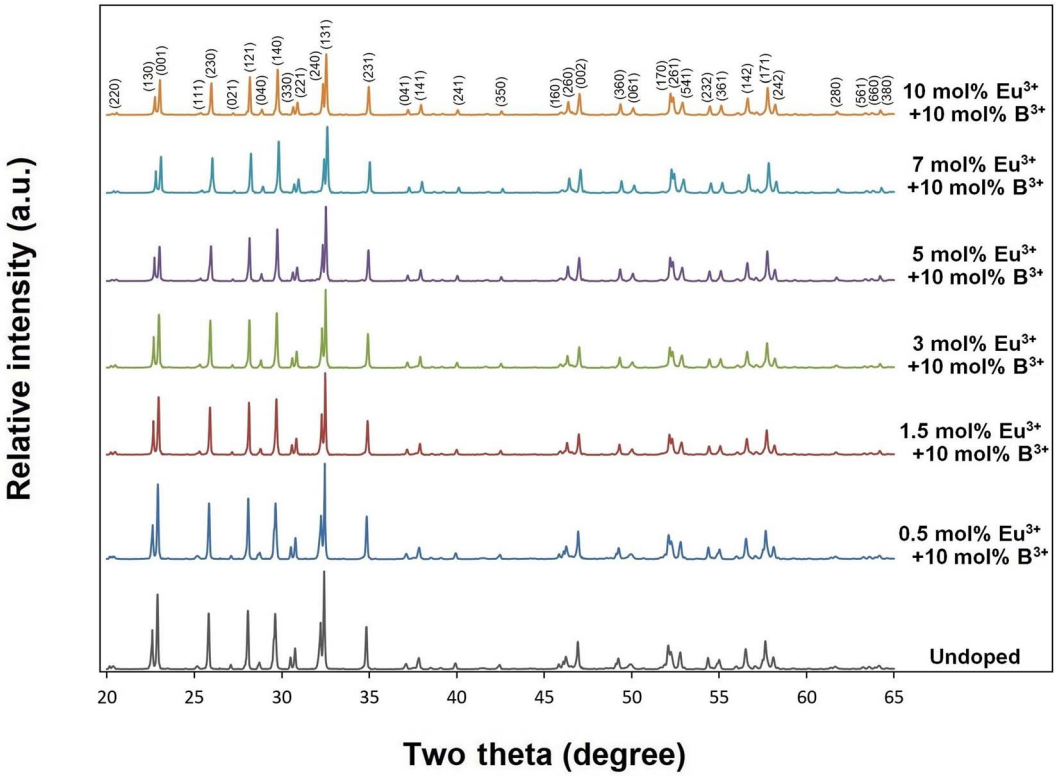

Fig. 3 XRD results of 10 mol% B^{3+}, and undoped, 0.5, 1.5, 3, 5, 7, 10 mol% Eu^{3+} co-doped $SrTa_2O_6$ samples.

SEM micrographs of $SrTa_2O_6$:xEu^{3+}, yB^{3+} samples for x = 5 mol% Eu^{3+}, y = 0, 5, 10, 20 mol% B^{3+} co-doped concentrations at 2000× and 10 000× magnifications under 15 kV accelerating voltage are shown in Fig. 4a–h, respectively. In SEM micrographs, it is seen that boron doping promotes agglomeration and growth, where grain boundaries are reduced or disappeared. In addition, grain size and agglomeration increase with increasing boron, as reported in the supporting study.[15] The increase in grain size can be seen in Fig. 4a, c, e and g at 2000× magnifications. More detail is shown in Fig. 4b, d, f and h at 10 000× magnifications, which are shown in the inset figures of Fig. 4a, c, e and g as yellow windows. Fig. 5a and b shows the XPS analysis of the 5 mol% Eu^{3+}, 20 mol% B^{3+} co-doped sample. In Fig. 5a, the binding energies of O1s, Sr3d, and Ta4f were identified at 529.26, 133.44, and 26.23 eV which belong to tantalum oxide structure, respectively. Also, the 1133 eV peak defines the europium dopant with Eu3d. In Fig. 5b, the binding energy of B1s is 189.59 eV. The broad spectrum in the range of about 187–192 eV shows that boron was incorporated into the structure. The binding energies of boron for the elemental and fully oxidized form (B_2O_3) are 187.2 eV (ref. 18) and 193.0 eV,[19,20] respectively. Accordingly, the broad B1s spectrum shows that interstitial B atoms can exist in different stoichiometric forms with oxygen in the structure.

3.2 Photoluminescence of $SrTa_2O_6$:xEu^{3+} and $SrTa_2O_6$:xEu^{3+}, yB^{3+} phosphors

Fig. 6a–c and 7a–c show PL excitations and emissions of orthorhombic tungsten bronze β-$SrTa_2O_6$ phosphors corresponding to the $SrTa_2O_6$:xEu^{3+} (x = 0.5, 1.5, 3, 5, 7, 10 mol% "without boron"), $SrTa_2O_6$:xEu^{3+}, yB^{3+} (x = 5 mol% "Eu^{3+} fixed", y = 0, 5, 10, 20 mol%), and $SrTa_2O_6$:xEu^{3+}, yB^{3+} (x = 0.5, 1.5, 3, 5, 7, 10 mol%, y = 10 mol% "boron fixed"), respectively. In Fig. 6a–c, PL excitations under 618 nm were assigned with $^7F_0 \rightarrow {}^5D_4$, $^7F_0 \rightarrow {}^5G_J$, $^7F_0 \rightarrow {}^5L_6$, $^7F_0 \rightarrow {}^5D_3$, and $^7F_0 \rightarrow {}^5D_2$ transitions, respectively. In Fig. 7a–c, PL emissions with 465 nm excitation were observed at $^5D_0 \rightarrow {}^7F_J$, ($J$ = 0, 1, 2, 3, 4, 5) corresponding to the Eu^{3+} transitions. Fig. 7a shows the PL spectra of $SrTa_2O_6$:xEu^{3+} (x = 0.5, 1.5, 3, 5, 7, 10) phosphors. The PL intensity reached its maximum value at 5 mol%, while the concentration quenching occurred at 7 and 10 mol%. Therefore, the concentration of the 5 mol% Eu^{3+} doped phosphor with the highest PL intensity was used to investigate the effect of different B^{3+} concentrations. The PL emissions of $SrTa_2O_6$:xEu^{3+}, yB^{3+} (x = 5, y = 0, 5, 10, 20 mol%) phosphors are given in Fig. 7b. The PL emission intensity increased up to 20 mol% B^{3+} concentration, while the intensity increase slightly slowed down over 10 mol%. By choosing 10 mol% B^{3+} doping ratio, $SrTa_2O_6$:xEu^{3+}, yB^{3+} (x = 0.5, 1.5, 3, 5, 7, 10 mol%, y = 10 mol%) phosphors were fabricated to compare with the $SrTa_2O_6$:xEu^{3+} (x = 0.5, 1.5, 3, 5, 7, 10 mol%) series. The PL emissions of $SrTa_2O_6$:xEu^{3+}, $0.1B^{3+}$ phosphors are presented in Fig. 7c, respectively. The PL emission intensity of $SrTa_2O_6$:xEu^{3+}, $0.1B^{3+}$ phosphors showed a nearly threefold increase compared to the $SrTa_2O_6$:xEu^{3+} series, which is compatible with the luminescence increase reported in the literature due to boron effect.

The charge transfer bands (CTB) under 618 nm wavelength of $^5D_0 \rightarrow {}^7F_2$ transition are shown in Fig. 6a–c. As seen in the

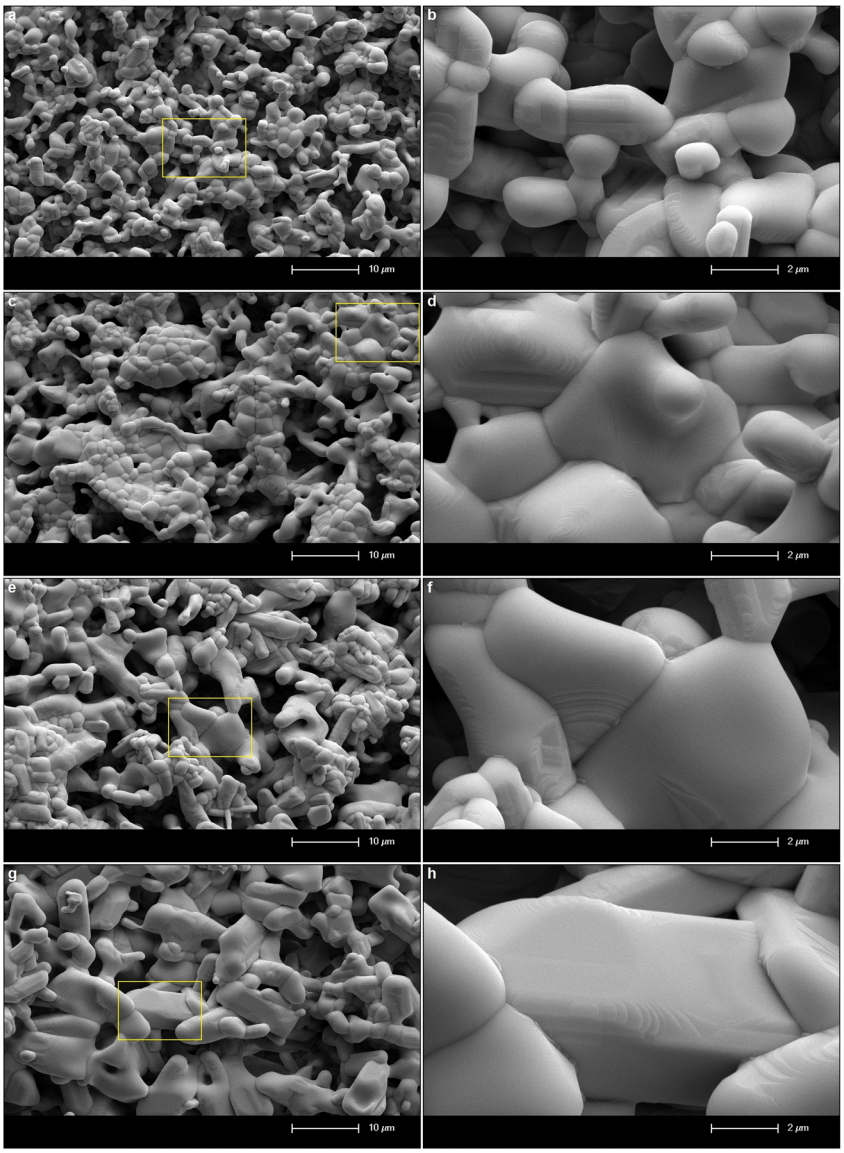

Fig. 4 SEM micrographs of 5 mol% Eu^{3+}, and different concentrations B^{3+} co-doped $SrTa_2O_6$ samples: (a and b) without B^{3+}, (c and d) 5 mol% B^{3+}, (e and f) 10 mol% B^{3+}, (g and h) 20 mol% B^{3+}, under 15 kV accelerating voltage at 2000× and 10 000× magnifications, respectively.

figures, the CTB peaks are over 300 nm, which is related to the ligand nature of the host structure.[21,22] It has been reported by many studies that the CTB energy is found at low energies or over 300 nm due to the ligand environment with highly coordinated A and B tunnels of the tungsten bronze structure.[6] Fig. 6b shows CT band position slightly affected with the increase in boron concentration, where the CTB peaks are at the wavelengths of 308.6, 310.4, 312.7, 314.2 nm for 0, 5, 10, 20 mol% B^{3+} concentrations, respectively. A shift to the lower energy in CTB position is also evident for the $SrTa_2O_6$:$x$$Eu^{3+}$, 0.1$B^{3+}$ phosphors (Fig. 6c) compared to $SrTa_2O_6$:$x$$Eu^{3+}$ series (Fig. 6a), where CTB positions are by average about 313 and 309 nm, respectively. The shift in CTB energy is related to the binding strength of valence electrons and the site of rare earth.[22] An atom with higher electronegativity will bind the oxygen 2p electron more strongly than an atom with lower electronegativity, where CT band will shift to a higher energy. The CTB energy will rise to a higher level, while the Eu^{3+} sites tend to be smaller. So, the CTB energy shift to the lower energy despite the high electronegativity of boron may be ascribed to the fact that the Eu^{3+} sites become larger. Another phenomenon is the relationship between CTB and hypersensitive transition. The inverse relationship between $^5D_0 \rightarrow {}^7F_2$ transition and CTB is highlighted, where the more intensity of $^5D_0 \rightarrow {}^7F_2$ transition indicates the lower energy of CTB.[22,23] In Fig. 7b, the asymmetry ratios for 0, 5, 10, and 20 mol% B^{3+} concentrations are 1.97, 2.34, 2.48, and 2.49, respectively. In Fig. 7a and c, the asymmetry values for Eu^{3+} doped and Eu^{3+}, B^{3+} co-doped phosphors varied in the range of 1.83–2.07, and 2.21–2.58, respectively. The results show that boron doping causes a decrease in CTB energy

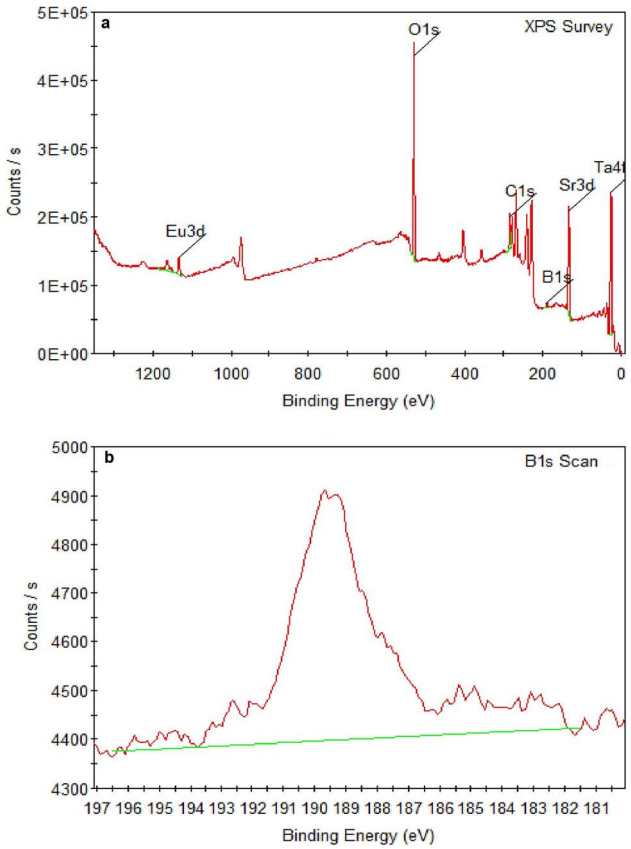

Fig. 5 XPS spectra of (a) 5 mol% Eu^{3+}, 20 mol% B^{3+} co-doped $SrTa_2O_6$ sample, (b) B1s.

and an increase in the $^5D_0 \rightarrow {}^7F_2$ transition intensity. On the other hand, the inverse correlation between CTB intensity and $^5D_0 \rightarrow {}^7F_2$ transition is previously observed in TTB-MTa_2O_6:-Eu^{3+} (Sr, Ba, Pb) phosphors. The trend of the $^5D_0 \rightarrow {}^7F_2$ transition is $BaTa_2O_6$:Eu^{3+} > $SrTa_2O_6$:Eu^{3+} > $PbTa_2O_6$:Eu^{3+} while trend of intensity of CTB and $^5D_0 \rightarrow {}^7F_1$ transition is reverse.[6] Hua *et al.*[24] compared the CINO:Eu^{3+}, SINO:Eu^{3+}, and BINO:Eu^{3+} phosphors. The CINO:Eu^{3+} phosphor has strong $^5D_0 \rightarrow {}^7F_2$ transition and weak CTB intensity, while there is an opposite effect for SINO:Eu^{3+}, BINO:Eu^{3+}. A similar phenomenon was also observed in this study. In Fig. 6c, $SrTa_2O_6$:xEu^{3+}, $0.1B^{3+}$ phosphors have a low CTB transition intensity and high asymmetry compared to $SrTa_2O_6$:xEu^{3+} phosphors (Fig. 6a). Since the formation of charge transfer bands or reduction of Eu^{3+} to Eu^{2+} is largely dependent on the nature of the ligands, the decrease in CTB density for the Eu^{3+}, B^{3+} co-doped phosphors may be associated with the decreased electron transfer from neighboring atoms to Eu^{3+} ions in the tungsten bronze host. It has been reported in many studies that the addition of boron contributes to the improvement of crystallization and increases luminescence. Besides, it is generally believed that improved crystallinity properties and low crystal field symmetry are advantageous for the luminescence of rare earth activators.[25] Consequently, the increase in asymmetry associated with the low crystal field symmetry of the Eu^{3+} sites as well as some enhancement crystallinity in Eu^{3+}, B^{3+} co-doped samples support the PL increase.

UV lamp photographs of the phosphors under 365 nm are given in Fig. 8a–c. As seen from the pictures, the Eu^{3+}, B^{3+} co-doped phosphors in Fig. 8c are brighter than Eu^{3+} doped samples in Fig. 8a. The increase in brightness with the increasing B^{3+} concentration is more evident after 10 mol%, which is given in Fig. 8b.

3.3 Judd–Ofelt analysis of $SrTa_2O_6$:$xEu^{3+}$and $SrTa_2O_6$:xEu^{3+}, $0.1B^{3+}$ phosphors

Judd–Ofelt (JO) theory explains the intensity of electron transitions in 4f shell of rare-earth ions using three parameters and describes their spectral properties.[26,27] The JO intensity parameters Ω_J (J = 2, 4, 6) from emission spectrum for Eu^{3+} can be determined by eqn (1):[28,29]

$$\Omega_J = \frac{S_{MD}(V_1{}^3)}{e^2(V_J{}^3)} \frac{9n^3}{n(n^2+2)^2} \frac{\int I_1(V_1)}{|\langle J\|U^J\|J'\rangle|^2 \int I_J(V_J)} \quad (1)$$

where V is the transition frequency, I_1 and I_J for $^5D_0 \rightarrow {}^7F_1$ and $^5D_0 \rightarrow {}^7F_J$ transitions are the integrated intensities, respectively, S_{MD} = 9.6 × 10^{-42} (esu^2 cm^2) is the magnetic dipole line strength,[6] n is the refractive index, $e = 4.803 \times 10^{-10}$ (esu) is the elementary charge, J and J' for the initial state and final state are the total angular momentum, respectively, $|\langle J\|U^J\|J\rangle|^2$ is the symbol of double reduced matrix elements for unit tensor operators. For all electric dipole (ED) transitions originating from the $^5D_0$ level, the reduced matrix elements are zero except for the $^5D_0 \rightarrow {}^7F_2$ ($U^2 = 0.0032$), $^5D_0 \rightarrow {}^7F_4$ ($U^4 = 0.0023$) and $^5D_0 \rightarrow {}^7F_6$ ($U^6 = 0.0002$) transitions.[28,29] The $^5D_0 \rightarrow {}^7F_J$ (J = 1, 2, 4, 6) transitions are used for the determination of the radiative transition probabilities while $^5D_0 \rightarrow {}^7F_J$ (J = 0, 3, 5) transitions are prohibited, and are not included JO calculation. The $^5D_0 \rightarrow {}^7F_6$ transition related to Ω_6 parameter was not included in the calculation because it could not be detected by PL in infrared region. However, the effect of this transition on the calculation is negligible, which has been reported in some studies.[28,29] The spontaneous transition probability (A) is related to its dipole strength which can be expressed as eqn (2):

$$A(J,J') = \frac{64\pi^4 V^3}{3h(2J+1)}[\chi_{ED}S_{ED} + \chi_{MD}S_{MD}] \quad (2)$$

where S_{ED} (electric dipole) and S_{MD} (magnetic dipole) are line strengths (in esu^2 cm^2), h is Planck constant. The electric dipole line strengths (S_{ED}) from the JO parameters can be calculated by eqn (3):

$$S_{ED}(J,J') = e^2 \sum_{J=2,4,6} \Omega_J |\langle J\|U^J\|J'\rangle|^2 \quad (3)$$

The χ_{ED} and χ_{MD} are the local field corrections for the ED and MD transitions which can be found by eqn (4) and (5) respectively:

$$\chi_{ED} = \frac{n(n^2+2)^2}{9} \quad (4)$$

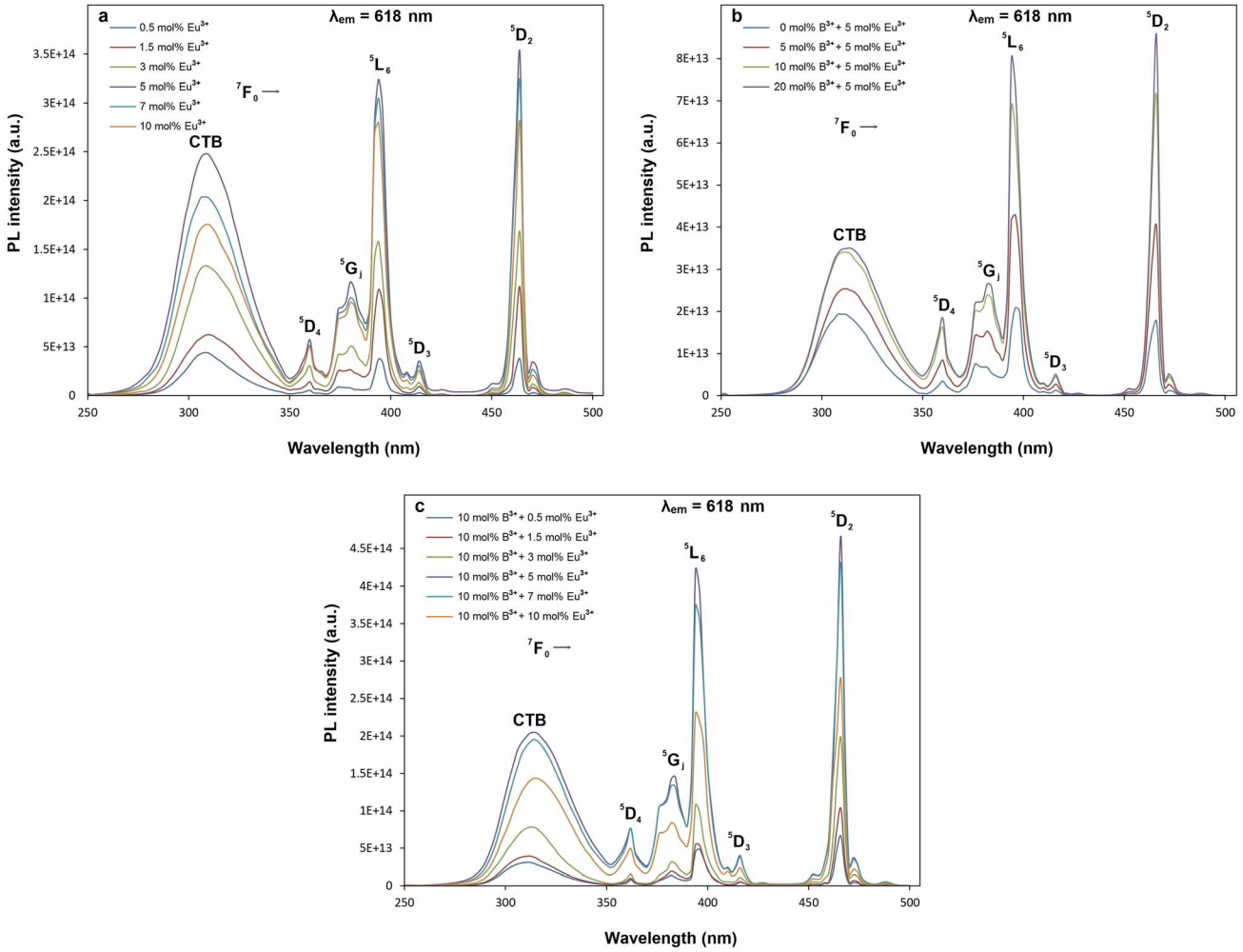

Fig. 6 PL excitation spectra and CT bands of (a) $SrTa_2O_6$:xEu^{3+}, (b) $SrTa_2O_6$:0.05Eu^{3+}, yB^{3+} (c) $SrTa_2O_6$:xEu^{3+}, 0.1B^{3+} phosphors corresponding to 618 nm emission.

$$\chi_{MD} = n^3 \quad (5)$$

where n is the refractive index of $SrTa_2O_6$ which was taken as 1.828 from ref. 6 and 7. The Judd–Ofelt intensity parameters (Ω_2, Ω_4) are given in Table 1. The parameter Ω_2, which is closely related to the hypersensitive electric dipole transition ($^5D_0 \rightarrow {}^7F_2$), indicates the covalency of the Eu–O bond character and the environmental changes of the Eu^{3+} ion.[6,7] The trend of the Ω_2 parameter is $SrTa_2O_6$:xEu^{3+}, 0.1B^{3+} > $SrTa_2O_6$:xEu^{3+}, where the slightly higher Ω_2 parameters of the boron doped phosphors indicate relatively high covalency of Eu–O and low local symmetry of Eu^{3+} sites. The parameter Ω_4 is related to the electron density of the surrounding ligands, where an increase in Ω_4 parameter indicates a decreased electron density.[28,29] The trend of the Ω_4 parameter is $SrTa_2O_6$:xEu^{3+}, 0.1B^{3+} > $SrTa_2O_6$:-xEu^{3+} wherein B^{3+} co-doped phosphors have relatively weak ligand density. The relatively high value of the Ω_4 parameter may be ascribed to the reduced charge transfer from the ligand ions to the Eu^{3+} ion, which supports the effect of boron to decrease the formation of CTB or the reduction of Eu^{3+} to Eu^{2+} and increase the $^5D_0 \rightarrow {}^7F_2$ transition intensity.

Fig. 9a–c shows the decay curves of $SrTa_2O_6$:xEu^{3+}, $SrTa_2O_6$:0.05Eu^{3+}, yB^{3+}, and $SrTa_2O_6$:xEu^{3+}, 0.1B^{3+} phosphors, respectively. The decay curves for $^5D_0 \rightarrow {}^7F_2$ transition were detected by the emission of 618 nm and excitation of 465 nm. Fluorescence bi-exponential decay curves can be produced using eqn (6):[27,28]

$$I_t = I_0 + I_1 \exp\frac{-t}{\tau_1} + I_2 \exp\frac{-t}{\tau_2} \quad (6)$$

where I_t is PL intensity, t is the time after excitation, I_0 is the background, I_1 and I_2 are luminescence intensities corresponding to τ_1 (long) and τ_2 (short) lifetimes, respectively. Accordingly, the average lifetime (τ) can be calculated through eqn (7):[28,30]

$$\tau = \frac{I_1\tau_1^2 + I_2\tau_2^2}{I_1\tau_1 + I_2\tau_2} \quad (7)$$

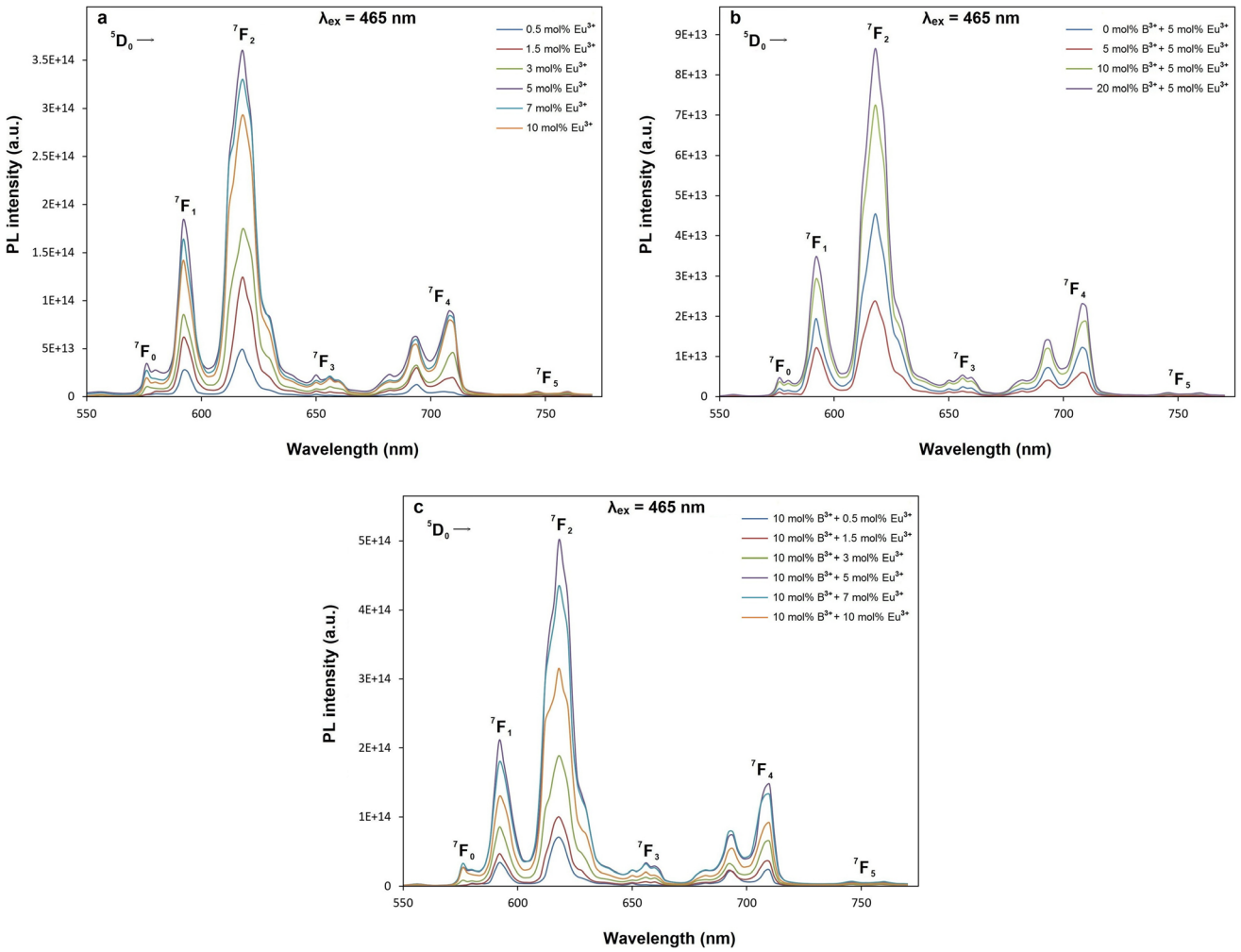

Fig. 7 PL emission spectra of (a) $SrTa_2O_6$:xEu^{3+}, (b) $SrTa_2O_6$:0.05Eu^{3+}, yB^{3+} (c) $SrTa_2O_6$:xEu^{3+}, 0.1B^{3+} phosphors with excitation of 465 nm.

The fitting parameters of bi-exponential decays for $SrTa_2O_6$:xEu^{3+}, $SrTa_2O_6$:xEu^{3+}, 0.1B^{3+}, and $SrTa_2O_6$:0.05Eu^{3+}, yB^{3+} are tabulated in Tables 2 and 3, where the average lifetimes varied between 1.178–0.904, 1.162–0.892, and 0.979–0.958 ms, respectively. In Table 2, for both phosphor series, a somewhat decrease was observed in the decay times with the increase of the Eu^{3+} concentration, and slightly low decay times were found in Eu^{3+}, B^{3+} co-doped samples compared to Eu^{3+} doped samples. The increased asymmetry supports the relatively lower average lifetimes of Eu^{3+}, B^{3+} co-doped samples.[31] The τ_1 (long) and τ_2 (short) lifetimes of the phosphors are given in Tables 2 and 3. In the literature, the authors made definitions of the long (τ_1) and short (τ_2) lifetimes, where the short decay component is associated with Eu^{3+} ions close to the surfaces of the particles, while the long decay component is related to Eu^{3+} ions in inner part of the particles.[32–35] Padlyak *et al.*[36] emphasized that the long lifetimes are characteristic of luminescence centers and belong to isolated Eu^{3+} centers in oxide glasses and polycrystalline samples while the short components belong to the Eu^{3+}–Eu^{3+} exchange-coupled pairs or small exchange-coupled Eu^{3+} clusters. On the other hand, Gupta *et al.*[37,38] highlighted that the long component and the short component are associated with high symmetry and low symmetry of Eu^{3+} ions, respectively. In Tables 2 and 3, there is an increase in τ_2 lifetimes and slight decrease in τ_1 lifetimes of Eu^{3+}, B^{3+} co-doped samples compared to Eu^{3+} doped phosphors. Accordingly, the change in the τ_1 and τ_2 lifetimes may be originated from the activation of Eu^{3+} luminescence centers at the particle surface rather than in the particle core/isolated centers. The variation in τ_2 an τ_1 lifetimes can be explained by the lowering of local symmetry of Eu^{3+} due to the presence of boron, which was previously expressed as an increase in $^5D_0 \rightarrow {}^7F_2/{}^5D_0 \rightarrow {}^7F_1$. The asymmetry variation of the Eu^{3+} doped samples is associated with the A, and B site occupation, charge balance, or some degree of crystal distortion in the tungsten bronze structure.[4,39] On the other hand, although there is some improvement in the crystal properties, the increase in the ratio of $^5D_0 \rightarrow {}^7F_2/{}^5D_0 \rightarrow {}^7F_1$ or the decrease in the local symmetry of Eu^{3+} ions is high in Eu^{3+}, B^{3+} co-doped samples. As mentioned in the XPS results, the fact that boron makes strong bonds with oxygen in the structure may be the reason for this difference (such as polarization). As another consequence,

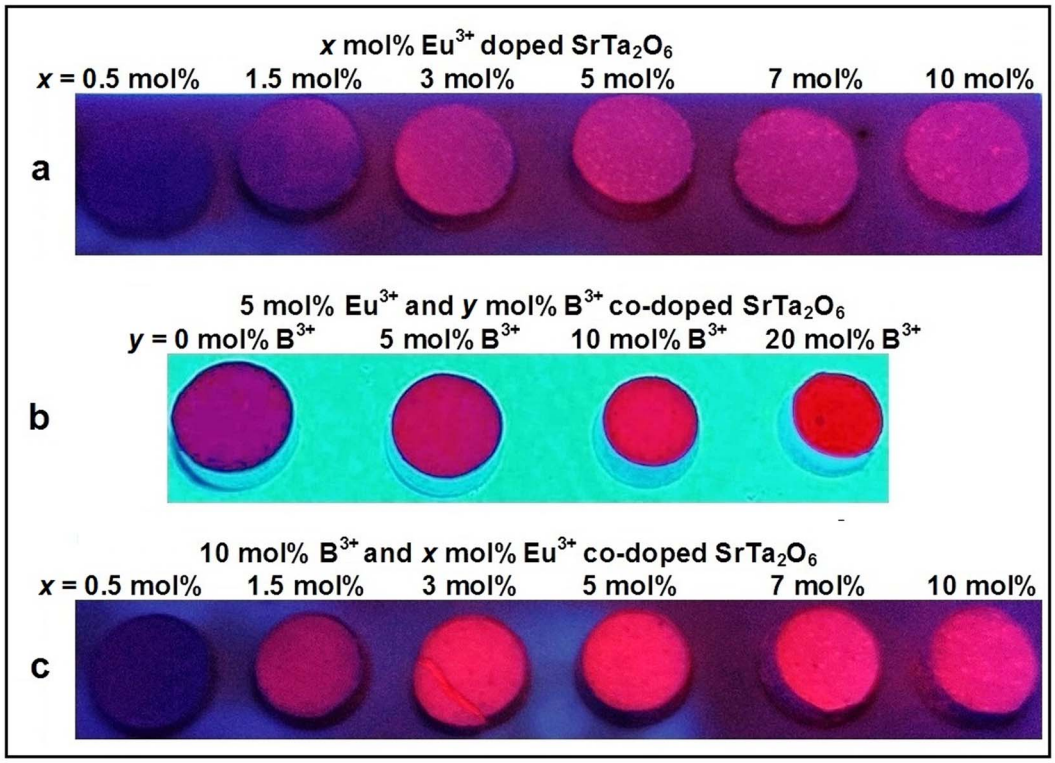

Fig. 8 UV lamp photos of (a) $SrTa_2O_6$:xEu^{3+}, (b) $SrTa_2O_6$:0.05Eu^{3+}, yB^{3+} (c) $SrTa_2O_6$:xEu^{3+}, 0.1B^{3+} phosphors at 365 nm.

Table 1 Judd–Ofelt intensity parameters (Ω_2, Ω_4) for $SrTa_2O_6$:xEu^{3+} (x = 0.5, 1.5, 3, 5, 7, 10 mol%) and $SrTa_2O_6$:xEu^{3+}, yB^{3+} (x = 0.5, 1.5, 3, 5, 7, 10 mol%, y = 10 mol%) phosphors

Eu^{3+} conc. (x mol%)	$SrTa_2O_6$:xEu^{3+}		$SrTa_2O_6$:xEu^{3+}, 0.1B^{3+}	
	Ω_2 ($\times 10^{-20}$ cm^2)	Ω_4 ($\times 10^{-20}$ cm^2)	Ω_2 ($\times 10^{-20}$ cm^2)	Ω_4 ($\times 10^{-20}$ cm^2)
0.5	2.963	1.670	3.586	2.800
1.5	3.315	1.764	3.692	3.101
3	3.343	1.943	3.806	3.130
5	3.201	1.906	4.070	2.887
7	3.292	2.018	4.162	3.055
10	3.367	2.196	4.183	2.913

increase of grain size in SEM micrographs is associated with the vitrification effect that accelerates agglomeration in boron grains. By evaluating the SEM micrographs and the decay components, it is seen that there is a correlation between grain growth and the increase in the short components. Similar behavior has been observed in Sm^{3+} doped $BaTa_2O_6$ phosphor, where grain growth with increasing sintering temperature leads to an increase in short components.[5] Although this requires further observation, it shows that grain growth may be related to the increase of Eu^{3+} luminescence centers on grain surfaces and a decrease in crystal field symmetry. The quantum efficiency (η_{QE}) of $^5D_0$ level can be found from the ratio of the average (observed) lifetime (τ) to the radiative lifetime (τ_r) by eqn (8):

$$\eta_{QE} = \frac{1}{\frac{A_r + A_{nr}}{A_r}} = \frac{\tau}{\tau_r} \quad (8)$$

where the radiative and nonradiative transitions of $^5D_0$ are A_r and A_{nr}, respectively. The radiative lifetimes (τ_r) and quantum efficiencies (η_{QE}) are tabulated in Table 2. The values of the η_{QE}% for $SrTa_2O_6$:xEu^{3+} and $SrTa_2O_6$:xEu^{3+}, 0.1B^{3+} phosphors varied between 36.03–30.30% and 42.72–36.08%, respectively. The η_{QE}% for Eu^{3+} and B^{3+} co-doped phosphors corresponds to an approximate increase of 15–21%. The quantum efficiency of the highest luminescent (or 0.05Eu^{3+}, 0.1B^{3+} co-doped) phosphor increased by about 21%. As mentioned in the previous sections, the low symmetry of the Eu^{3+} sites and some

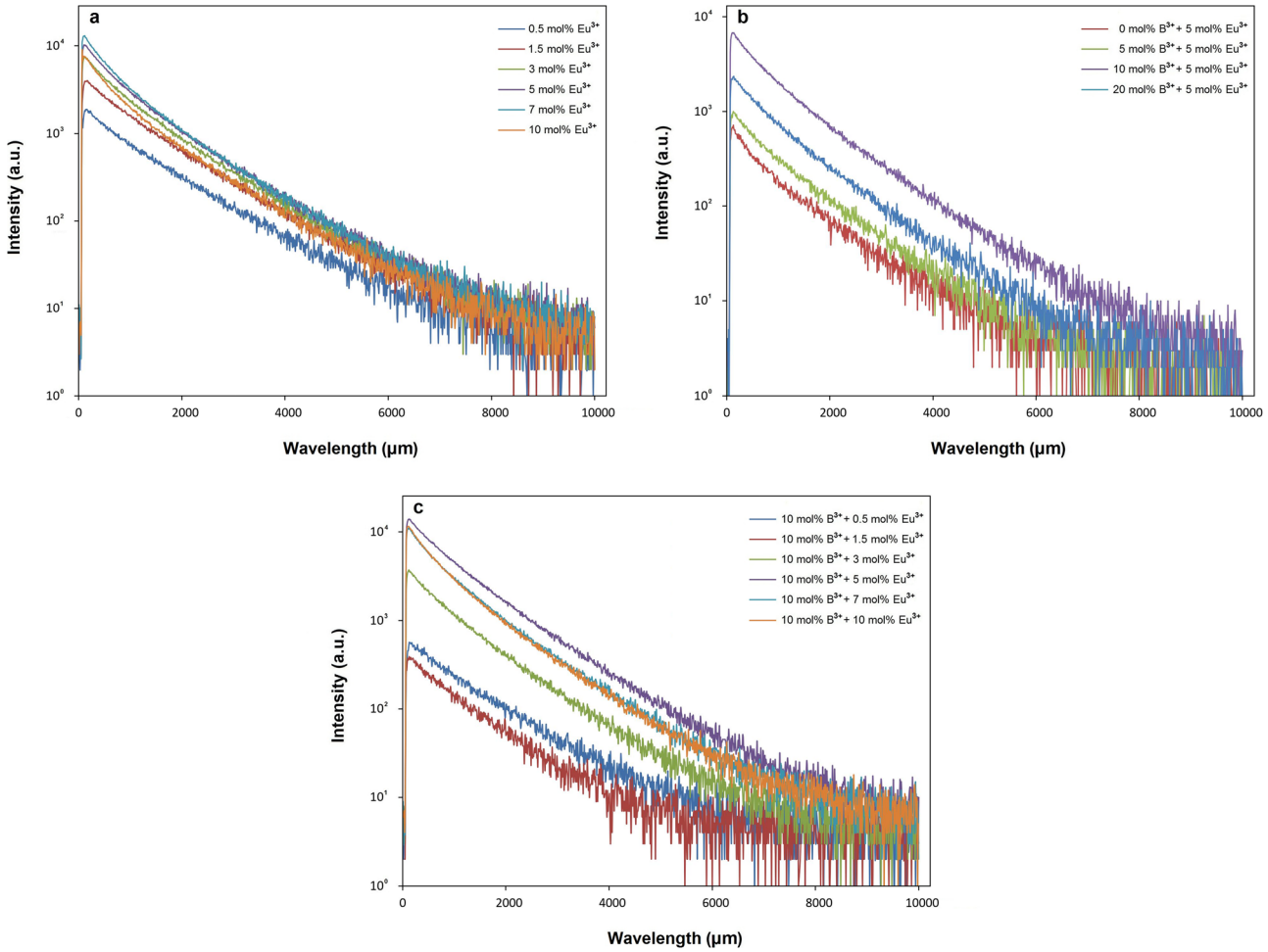

Fig. 9 Decay curves of (a) $SrTa_2O_6$:xEu^{3+}, (b) $SrTa_2O_6$:0.05Eu^{3+}, yB^{3+} (c) $SrTa_2O_6$:xEu^{3+}, 0.1B^{3+} phosphors with emission of 618 nm and excitation of 465 nm.

Table 2 Long (τ_1) and short (τ_2) lifetimes, average (observed) lifetimes (τ), radiative lifetimes (τr), quantum efficiencies (η_{QE}) and chi-square (x^2) values for $SrTa_2O_6$:xEu^{3+} (x = 0.5, 1.5, 3, 5, 7, 10 mol%) and $SrTa_2O_6$:xEu^{3+}, yB^{3+} (x = 0.5, 1.5, 3, 5, 7, 10 mol%, y = 10 mol%) phosphors

	$SrTa_2O_6$:xEu^{3+}						$SrTa_2O_6$:xEu^{3+}, 0.1B^{3+}					
Eu^{3+} conc. (x mol%)	τ_1 (ms)	τ_2 (ms)	τ (ms)	τ_r (ms)	η_{QE} (%)	x^2	τ_1 (ms)	τ_2 (ms)	τ (ms)	τ_r (ms)	η_{QE} (%)	x^2
0.5	1.293	0.504	1.178	3.283	35.88	1.190	1.259	0.429	1.162	2.720	42.72	1.106
1.5	1.274	0.319	1.101	3.056	36.03	1.151	1.205	0.521	1.086	2.619	41.47	1.196
3	1.198	0.421	1.012	3.025	33.45	1.179	1.183	0.452	1.003	2.570	39.03	1.108
5	1.147	0.462	0.978	3.110	31.45	1.156	1.135	0.425	0.959	2.516	38.12	1.225
7	1.112	0.387	0.919	3.033	30.30	1.142	1.104	0.437	0.902	2.456	36.73	1.208
10	1.148	0.395	0.904	2.952	30.62	1.360	1.113	0.423	0.892	2.472	36.08	1.194
Avg	1.195	0.415	1.015	3.077	32.96	—	1.167	0.448	1.001	2.559	39.03	—

Table 3 Long (τ_1) and short (τ_2) lifetimes, average (observed) lifetimes (τ) and chi-square (x^2) values for $SrTa_2O_6$:xEu^{3+}, yB^{3+} (x = 5 mol%, y = 0, 5, 10, 20 mol%) phosphors

	$SrTa_2O_6$:0.1Eu^{3+}			
B^{3+} conc. (y mol%)	τ_1 (ms)	τ_2 (ms)	τ (ms)	x^2
0	1.131	0.306	0.979	1.057
5	1.111	0.346	0.991	1.003
10	1.147	0.436	0.950	1.178
20	1.110	0.440	0.958	1.107

enhancement in crystal structure properties are likely to increase the luminescence efficiency.

4. Conclusion

The effect of boron on the structural and spectral properties was studied by using Eu^{3+} doped orthorhombic β-$SrTa_2O_6$ fabricated by solid-state method at 1400 °C for 20 h. The phase structure of

all the ceramics preserved up to 10 mol%, and the Eu^{3+}, B^{3+} co-doped samples have relatively slightly better crystallinity. SEM micrographs showed that the presence of boron promoted agglomeration and growth in grains. The increment in boron concentration led to an increase in PL up to 20 mol%, and the increase of PL may be related to the low symmetry of Eu^{3+} ions and the improvement of crystal properties. In Eu^{3+}, B^{3+} co-doped samples, the charge transfer band slightly shifted to the lower energy and asymmetry of phosphor increased. The trend of Judd–Ofelt (Ω_2, Ω_4) parameters was $SrTa_2O_6$:$x$$Eu^{3+}$, $0.1B^{3+}$ > $SrTa_2O_6$:$x$$Eu^{3+}$. The high values of the Ω_2, and Ω_4 for Eu^{3+}, B^{3+} co-doped phosphors related to a covalent Eu–O bond character with low symmetry of the Eu^{3+} ions and a reduced electron density in the ligands, respectively. While the increase of Eu^{3+} causes a slight decrease in the decay times, the decrease is slightly more in the Eu^{3+}, B^{3+} co-doped samples. The increase in τ_2 lifetimes may be associated with the activation of the Eu^{3+} luminescence centers at the grain surface and near the surface. The quantum efficiencies of the Eu^{3+}, B^{3+} co-doped phosphors increased between 15–21%.

Conflicts of interest

There are no conflicts to declare.

References

1 K. Binnemans, *Coord. Chem. Rev.*, 2015, **295**, 1–45.
2 C. G. Walrand and K. Binnemans, *Handbook on the Physics and Chemistry of Rare Earths*, Elsevier, Belgium, 1998, pp. 101–264.
3 M. İlhan and İ. Ç. Keskin, *Physica B*, 2020, **85**, 412106.
4 M. İlhan, *Solid State Sci.*, 2014, **38**, 160–168.
5 M. İlhan and L. F. Güleryüz, *Chem. Pap.*, 2022, **76**, 6963–6974.
6 M. İlhan, M. İ. Katı, İ. Ç. Keskin and L. F. Güleryüz, *J. Alloys Compd.*, 2022, **901**, 163626.
7 M. İlhan, İ. Ç. Keskin, L. F. Güleryüz and M. İ. Katı, *J. Mater. Sci.: Mater. Electron.*, 2022, **33**, 16606–16620.
8 E. Lee, C. H. Park, D. P. Shoemaker, M. Avdeev and Y. I. Kim, *J. Solid State Chem.*, 2012, **191**, 232–238.
9 J. Y. Kim and Y. I. Kim, *J. Ceram. Soc. Jpn.*, 2015, **123**, 419–422.
10 H. Kato and A. Kudo, *Chem. Lett.*, 1999, **28**, 1207–1208.
11 Y. Huang, Q. Feng, Y. Yang and H. J. Seo, *Phys. Lett. A*, 2005, **336**, 490–497.
12 D. Zhao, Y. Yu, C. Cao, J. Wang, E. Wang and Y. Cao, *Appl. Surf. Sci.*, 2015, **345**, 67–71.
13 N. Lu, H. Zhao, J. Li, X. Quan and S. Chen, *Sep. Purif. Technol.*, 2008, **62**, 668–673.
14 E. Finazzi, C. D. Valentin and G. Pacchioni, *J. Phys. Chem. C*, 2009, **133**, 220–228.
15 V. Vitola, I. Bite, D. Millers, A. Zolotarjovs, K. Laganovska, K. Smits and A. Spustaka, *Ceram. Int.*, 2020, **46**, 26377–26381.
16 A. S. Başak, M. K. Ekmekçi, M. Erdem, M. İlhan and A. Mergen, *J. Fluoresc.*, 2016, **26**, 719–724.
17 J. Kaduk and W. Wong-Ng, *International Center for Diffraction Data*, PDF code 00-051-1683.
18 W. E. Moddeman, A. R. Burke, W. C. Bowling and D. S. Foose, *Surf. Interface Anal.*, 1989, **14**, 224.
19 D. H. Quinones, A. Rey, P. M. Álvarez, F. J. Beltrán and G. L. Puma, *Appl. Catal., B*, 2015, **178**, 74–81.
20 W. Zhang, T. Hu, B. Yang, P. Sun and H. He, *J. Adv. Oxid. Technol.*, 2013, **16**, 261–267.
21 G. Blasse, *J. Solid State Chem.*, 1972, **4**, 52–54.
22 P. Dorenbos, *J. Lumin.*, 2005, **111**, 89–104.
23 D. E. Henrie, R. L. Fellows and G. R. Choppin, *Coord. Chem. Rev.*, 1976, **18**, 199–224.
24 Y. Hua, T. Wang, J. S. Yu, W. Ran and L. Li, *Inorg. Chem. Front.*, 2022, **9**, 6211–6224.
25 Q. Shao, H. Zhang, J. Dai, C. Yang, X. Chen, G. Feng and S. Zhou, *CrystEngComm*, 2020, **22**, 1359.
26 B. R. Judd, *Phys. Rev.*, 1962, **127**, 750.
27 G. S. Ofelt, *J. Chem. Phys.*, 1962, **37**, 511.
28 M. İlhan, M. K. Ekmekçi and İ. Ç. Keskin, *RSC Adv.*, 2021, **11**, 10451–10462.
29 M. İlhan and İ. Ç. Keskin, *Phys. Chem. Chem. Phys.*, 2020, **22**, 19769–19778.
30 R. Saraf, C. Shivakumara, S. Behera, H. Nagabhushana and N. Dhananjaya, *RSC Adv.*, 2015, **5**, 4109.
31 G. Blasse, *J. Phys. Chem. Solids*, 1989, **50**, 99.
32 J. W. Stouwdam and F. C. M. van Veggel, *Nano Lett.*, 2002, **2**, 733–737.
33 V. Sudarsan, F. C. J. M. van Veggel, R. A. Herring and M. Raudseppc, *J. Mater. Chem.*, 2005, **15**, 1332.
34 N. Yaiphaba, R. S. Ningthoujam, N. S. Singh, R. K. Vatsa, N. R. Singh, S. Dhara, N. L. Misra and R. Tewari, *J. Appl. Phys.*, 2010, **107**, 034301.
35 A. K. Parchur and R. S. Ningthoujam, *RSC Adv.*, 2012, **2**, 10859–10868.
36 B. Padlyak, M. Grinberg, B. Kukliński, Y. Oseledchik, O. Smyrnov, D. Kudryavtcev and A. Prosvirnin, *Opt. Appl.*, 2010, **2**, 413–426.
37 S. K. Gupta, B. Modak, M. Tyagi, N. S. Rawat, P. Modak and K. Sudarshan, *ACS Omega*, 2022, **7**, 5311–5323.
38 S. K. Gupta, C. Reghukumar and R. M. Kadam, *RSC Adv.*, 2016, **6**, 53614–53624.
39 M. İlhan, M. K. Ekmekçi, A. Mergen and C. Yaman, *J. Fluoresc.*, 2016, **26**, 1671–1678.